# Raman and photoluminescence spectra of two-dimensional nanocrystallites of monolayer $WS_2$ and $WSe_2$



2016 2D Mater. 3 025016

(http://iopscience.iop.org/2053-1583/3/2/025016)

2D Materials

RECEIVED
20 September 2015

REVISED
22 March 2016

ACCEPTED FOR PUBLICATION
6 April 2016

PUBLISHED
28 April 2016

PAPER

# Raman and photoluminescence spectra of two-dimensional nanocrystallites of monolayer $WS_2$ and $WSe_2$

**Wei Shi, Miao-Ling Lin, Qing-Hai Tan, Xiao-Fen Qiao, Jun Zhang and Ping-Heng Tan**

State Key Laboratory of Superlattices and Microstructures, Institute of Semiconductors, Chinese Academy of Sciences, Beijing 100083, People's Republic of China

**E-mail:** phtan@semi.ac.cn

**Keywords:** phonon quantum confinement, Raman spectroscopy, photoluminescence, two-dimensional nanocrystallites, two-dimensional material, transition metal dichalcogenides

## Abstract

Defects strongly modify optical properties in pristine and nanostructured two-dimensional (2D) materials. The ion implantation technique can be used to gradually introduce defects in semiconductor to obtain nanocrystallites (NCs) with different domain sizes. Here, we present a detailed study on the Raman and photoluminescence spectra of 2D NCs of monolayer $WS_2$ (1L $WS_2$) and 1L $WSe_2$ prepared by ion implantation. With increasing ion dosages, both $E'$ and $A_1'$ modes of 1L $WS_2$ exhibit a downshift in frequency and an asymmetrical broadening toward lower frequency, while the $A_1'$ mode in 1L $WSe_2$ NCs exhibits an opposite behavior, showing asymmetrical broadening and peak shift toward higher frequency. This behavior is well understood by phonon quantum confinement of the out-of-plane optical branch whose frequency displays a minimum at Γ in pristine 1L $WSe_2$. After the ion implantation, phonons from the Brillouin zone boundary are revealed in the Raman spectra, and the corresponding assignments are identified by resonant Raman spectra at low temperature. The defects can act as trapping centers of free carriers, which result in a sharp decrease of photoluminescence (PL) emission from A exciton with increasing ion dosage. The PL peak from A-exciton in both 1L $WS_2$ and 1L $WSe_2$ NCs blueshifts with increasing the ion dosage due to the quantum confinement effect of smaller NC size. The ion-implantation results in a new emission peak of defect-bound neutral excitons below the A-exciton peak in both 1L $WS_2$ and 1L $WSe_2$ NCs. Its relative intensity to the A exciton increases with increasing the ion dosage and finally vanishes along with the A exciton. These results offer a route toward tailoring the optical properties of 2D materials by controlling the size of 2D NCs.

## 1. Introduction

Two-dimensional (2D) transition metal dichalcogenides (TMDs) sparked wide interests in the world due to their remarkable electronic and optical properties [1, 2]. The 2D features, sizable bandgaps and recent advances in the synthesis, characterization and device fabrication of the $MX_2$($M$ = Mo, W; $X$ = S, Se, Te) make TMDs attractive in nanoelectronics and optoelectronics [3, 4]. However, defects may be introduced during the synthesis and fabrication process. The quality of the crystal lattice will be significantly affected by structure defects, thus affects the $MX_2$-based devices performance. Lattice point defects can act as very efficient trapping centers for electrons, holes and excitons in semiconductors, and crucially influence the transport and optical properties of the host material [5, 6]. Moreover, defects can break the perfect lattice structure of crystal and form small-sized nanocrystallites (NCs) [7, 8]. The fundamental momentum conservation requirement $q \sim 0$ for the Raman process is relaxed for NCs and phonons away from Γ will be involved in the Raman scattering [9]. This usually gives a downshift and asymmetric broadening of the Raman peak for various NCs, such as nanowires, nanodots and defective graphene [4, 9–18]. It becomes a common concept that the Raman peaks in NCs will exhibit a redshift in frequency with decreasing the NCs domain size. However, for the 1L-$MoS_2$ NCs, [4, 18] with decreasing the NC domain

size, the E′ mode exhibits a downshift in frequency and asymmetrical broadening toward lower frequency, while the $A_1'$ mode exhibits an opposite behavior, showing asymmetrical broadening and peak shift toward higher frequency. The results are attributed to the opposite phonon dispersion trends away from the Γ point for the two modes [4, 18].

1L $WS_2$ and 1L $WSe_2$ are another two typical TMD materials. The Raman spectrum of 1L $WS_2$ is dominated by two first-order peaks assigned as E′ (357.7 $cm^{-1}$) and $A_1'$ (419 $cm^{-1}$), while the E′ and $A_1'$ modes in 1L $WSe_2$ are degenerate at 250 $cm^{-1}$ [19]. The resonant Raman scattering (RRS) has been recognized as an important method for probing phonon spectra of 1L and multilayer TMDs [4, 20–23]. It provides an avenue to get insight into multi-phonon process due to the relaxation of selection rules and a huge amplification of Raman intensity. Moreover, it has been reported that phonons from the boundary of Brillouin zone (BZ) may be activated by defects, [4, 17, 18, 24] which paves a way to get rich phonon information from the intriguing 2D materials.

In this work the ion-implantation technique is used to gradually introduce defects in 1L $WS_2$ and 1L $WSe_2$ to obtain corresponding NCs with different sizes. We present a detailed report on the Raman and photoluminescence (PL) spectra of 1L $WS_2$ and 1L $WSe_2$ NCs. For 1L $WS_2$, both E′ and $A_1'$ modes show a redshift with increasing ion dosage, while the $A_1'$ of 1L $WSe_2$ shifts toward higher frequency side with increasing ion dosage. Besides the E′ and $A_1'$ modes shift and broadening, several defect-induced peaks arising from overtone, combination of phonons at BZ boundary in 1L $WS_2$ are observed. The corresponding assignments are further confirmed by RRS at low temperature. Both the experimental results of 1L $WS_2$ and 1L $WSe_2$ NCs can be well reproduced by the phonon confinement model originally proposed by Richter, Wang and Ley (hereafter this model is referred as the RWL model) [9]. We also studied the role of defects on the PL of 1L $WS_2$ and 1L $WSe_2$ NCs. A defect-related peak below the free A-exciton peak is observed for both 1L $WS_2$ and 1L $WSe_2$ NCs, which is attributed to the defect-induced bound-exciton. The intensity of the defect-related peak relative to that of A exciton increases with increasing ion dosage and finally vanishes along with the A exciton, revealing the evolution of size and lattice structure of 1L $WS_2$ and 1L $WSe_2$ NCs with increasing ion dosage.

## 2. Experimental details

1L $WS_2$ and 1L $WSe_2$ flakes were prepared from bulk crystals onto the Si substrates capped by a 90 nm thick $SiO_2$ layer using the mechanical exfoliation method. The layer number ($N$) was identified by ultralow-frequency Raman spectroscopy and PL spectra [25]. In the experiments, all the optical measurements were undertaken in backscattering configuration using a Jobin-Yvon HR800 system equipped with a liquid-nitrogen-cooled charge-coupled detector. The Raman measurements were undertaken with a × 100 objective lens (NA = 0.90) and a 1800 lines $mm^{-1}$ grating at room temperature, while a × 50 long-working-distance objective lens (NA = 0.55) was used for Raman measurements at low temperature. The laser excitation wavelengths are 594 nm from a He–Ne laser; 568, 530.8 and 514.5 nm from a $Kr^+$ laser; and 488 nm from an $Ar^+$ laser. A low laser power of ~40 μW is used to avoid heating and damaging. The Montana cryostat system was employed to cool the samples down to 5 K under a vacuum of 0.4 mTorr. Mignuzzi *et al* introduced defects in monolayer $MoS_2$ in an extremely controlled manner using a time-of-flight secondary ion mass spectrometry instrument with an ion dose distribution uniform to better than 99.9999% [18]. In the present work, the $Ar^+$ implantation experiment was performed with an LC-4 type vacuum system. Several works on bulk graphite and few layer graphenes had been completed based on this system [26, 27]. The kinetic energy of $Ar^+$ ions is 100 keV. The samples were subjected to nine different ion dosages, $1 \times 10^{12}$, $5 \times 10^{12}$, $1 \times 10^{13}$, $3 \times 10^{13}$, $5 \times 10^{13}$, $8 \times 10^{13}$, $1 \times 10^{14}$, $3 \times 10^{14}$ and $5 \times 10^{14}$ $cm^{-2}$, respectively. The corresponding samples are denoted as #$n$-NCa for ion-implanted 1L $WS_2$ and #$n$-NCb for ion-implanted 1L $WSe_2$, respectively, where $n = 1, 2, 3, 4, 5, 6, 7, 8, 9$. The domain size was analyzed by fitting the E′ and $A_1'$ mode of 1L $WS_2$ and 1L $WSe_2$ NCs at each ion dosage.

## 3. Results and discussions

Figure 1 shows the representative Raman spectra of 1L $WS_2$ and 1L $WSe_2$ exposed to different ion dosages. For both 1L $WS_2$ and 1L $WSe_2$, the intrinsic E′ mode is usually overlapped by the 2LA(M) mode in the Raman spectra under resonant condition [4, 23]. In order to get the intrinsic E′ and $A_1'$ modes, the 488 nm excitation is used to obtain the non-resonant Raman signal of these pristine and ion-implanted samples. The ion-implantation results in the formation of NCs of 1L $WS_2$ and 1L $WSe_2$. Figure 1(a) depicts the Raman spectra of pristine and NCs of 1L $WS_2$. With increasing ion dosage, a decrease in intensity and a redshift in frequency are observed for both E′ and $A_1'$ modes, indicating that the crystal quality become worse and worse with increasing ion dosage. Moreover, both of them have an asymmetric tail towards lower wavenumber side with increasing ion dosage. When the ion dosage increases from 0 (pristine) to $1 \times 10^{14}$ (#7-NCa), the E′ mode exhibits a refshift of 1.1 $cm^{-1}$ while the $A_1'$ mode redshifts 1.5 $cm^{-1}$. Figure 1(b) depicts the spectra of 1L $WSe_2$ NCs. The E′ and $A_1'$ modes are degenerated in pristine 1L $WSe_2$ [4, 19]. A polarization Raman measurement indicates that the intensity of

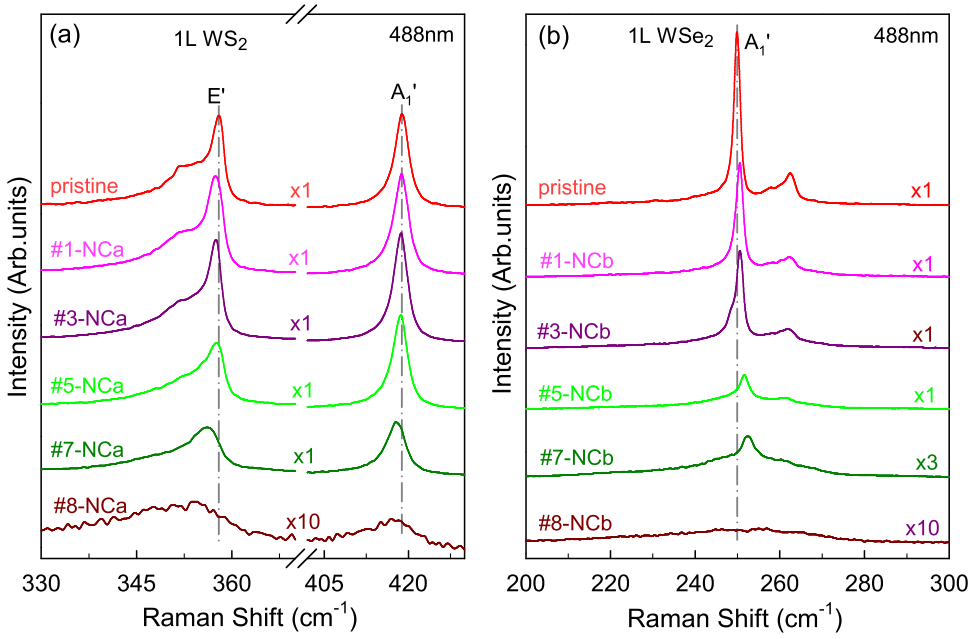


**Figure 1.** Evolution of Raman spectra of ion-implanted (a) 1L $WS_2$ and (b) 1L $WSe_2$ with different ion dosages in the $E'$ and $A_1'$ ranges. The dotted lines are guides to the eye. The excitation wavelength is 488 nm.

the $E'$ mode is only about 1/8 of that of the $A_1'$ mode, and thus, the evolution of Raman spectra with increasing ion dosage is dominated by the $A_1'$ mode. Obviously, the $A_1'$ mode of 1L $WSe_2$ NCs exhibits an opposite shift with respect to 1L $WS_2$ NCs with increasing ion dosage. The $A_1'$ mode of #7-NCb blueshifts 2.5 $cm^{-1}$ with respect to the pristine one. The intensity of the $A_1'$ mode in 1L $WSe_2$ NCs decrease more quickly than that of Raman modes in 1L $WS_2$ NCs with increasing ion dosage. This indicates that the lattice structure of 1L $WSe_2$ is easily damaged by ion implantation with respect to 1L $WS_2$. For #8-NCa and #8-NCb, the $E'$ and $A_1'$ modes almost vanish with only very broadened and weak signal.

Figure 1 suggests that ion-implantation results in peak shift, broadening and profile asymmetry of the Raman bands of 1L $WS_2$ NCs and 1L $WSe_2$ NCs. The softening in frequency and an asymmetric tail towards the lower frequency side of the $E'$ and $A_1'$ modes in 1L $WS_2$ NCs had been observed in various NCs [9, 11–14, 16]. NCs induced by ion implantation in 1L $WS_2$ can make the fundamental $q \sim 0$ Raman selection rule relaxed, allowing participation of phonons away from $\Gamma$. This phonon uncertainty in NCs can be taken into account in the Raman process by a phonon weighting function $W(r, L)$. A Gaussian-type profile of $W(r, L)$ has been widely used in NCs as follows: [28, 29]

$$W(r, L) = \exp(-\alpha r^2/L^2), \quad (1)$$

where $L$ is the domain size of NCs, $\alpha$ is an adjustable confinement coefficient to determine how fast the phonon amplitude decays to the NC boundary. $\alpha = 8\pi^2$ has been widely used in the literatures, [9, 12–14] which gives too strong confinement. Therefore, other $\alpha$ values had also been used to understand Raman spectra of various NCs [4, 12, 13, 18].

In order to quantitatively analyze peak shift and asymmetrical broadening of Raman peaks in NCs, RWL model has been proposed based on $W(r, L)$. The corresponding Raman intensity in the RWL model is given by

$$I(\omega) = \int \frac{|C(0, \mathbf{q})|^2}{(\omega - \omega(\mathbf{q}))^2 + (\Gamma_0/2)^2} \mathrm{d}^3q, \quad (2)$$

where $|C(0, \mathbf{q})|^2$ is a Fourier coefficient of $W(r, L)$, $\Gamma_0$ is the natural broadening, $\omega(q)$ is the phonon dispersion curve. The integration is over the BZ. In the case of a nanodot, $\mathrm{d}^3q \propto q^2\,\mathrm{d}q$, while for a nanowire with length $\gg$ diameter $\mathrm{d}^3q \propto q\mathrm{d}q$. For 2D NCs with a domain size of $L_D$, $\mathrm{d}^3q = 2\pi q\,\mathrm{d}q$. Once $|C(0, \mathbf{q})|^2$ is chosen for 2D NCs, for an example, to be $\exp(-q^2L_D^2/2\alpha)$ resulting from a Gaussian-type profile of $W(r, L)$ in equation (1), the Raman lineshape of 2D NCs is composed of superimposing Lorentzian peaks centered at $\omega(q)$ weighted by $C(0, \mathbf{q})$ and is given by

$$I(\omega) = \int \frac{\exp(-q^2L_D^2/2\alpha)}{(\omega - \omega(\mathbf{q}))^2 + (\Gamma_0/2)^2} 2\pi q\,\mathrm{d}q. \quad (3)$$

The phonon confinement effect in 2D NCs described by equation (3) quantifies the $q \neq 0$ phonons participating in the scattering. If two branches of phonon dispersion curves of a 2D crystal degenerated at $\Gamma$ contribute to a Raman mode, $q \neq 0$ phonons of two branches must be taken into account to reveal the effect of phonon confinement on the lineshape of Raman modes. The $A_1'$ mode is from an out-of-plane optical ($ZO_2$) branch. The $E'$ mode is from two in-

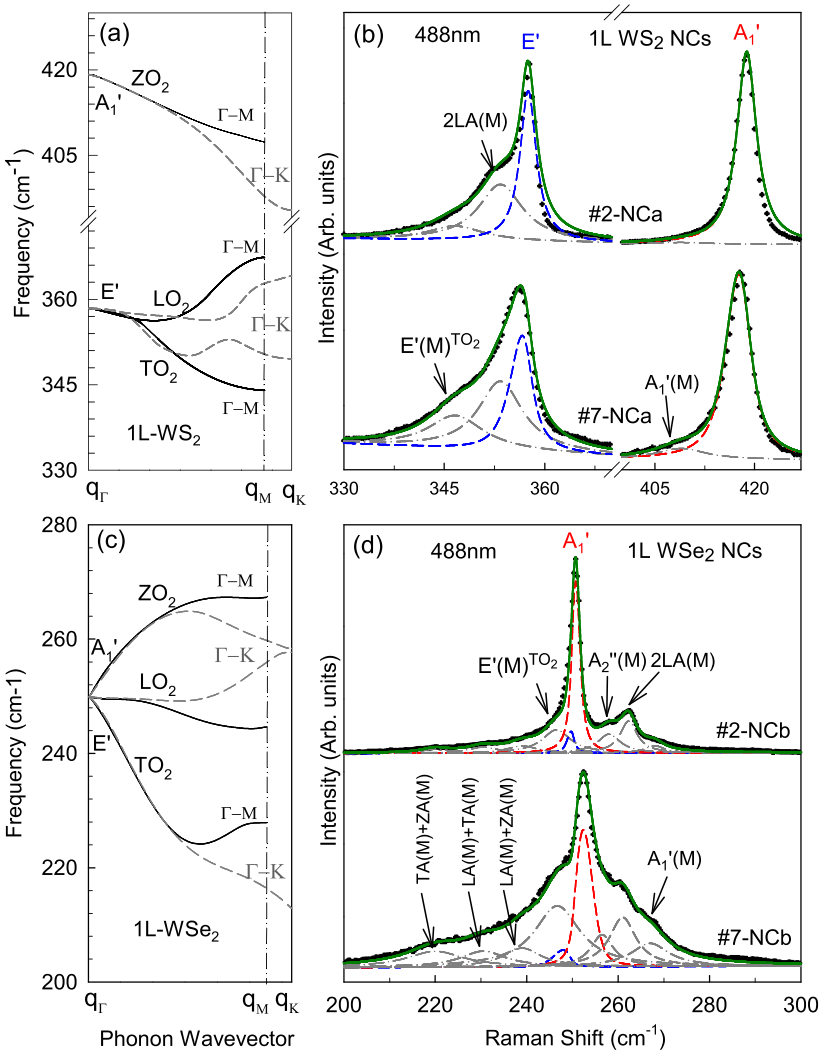


**Figure 2.** (a) The phonon branches [30] of 1L $WS_2$ related with the E′ and $A_1'$ modes. (b) The experimental (crosses) and fitted (green solid lines) results of two 1L $WS_2$ NCs. (c) The phonon branches [31] of 1L $WSe_2$ related with the E′ and $A_1'$ modes. (d) The experimental (crosses) and fitted (green solid lines) results of two 1L $WSe_2$ NCs. The blue and red dashed lines are the calculated curves of the E′ and $A_1'$ modes, respectively, and the gray dashed–dotted lines are fits with Lorentzian peaks to the zone-boundary peaks. The spectra are normalized to $A_1'$.

plane optical branches, which are degenerated at Γ and split into one in-plane longitudinal optical ($LO_2$) branch and one in-plane transverse optical ($TO_2$) branch. The dispersions of 1L $WS_2$ in the E′ and $A_1'$ region are taken from the work of Molina *et al* [30] as depicted in figure 2(a). The dispersion is anisotropic along Γ–M and Γ–K. To minimize this effect on the experimental results, each branch is obtained by averaging the dispersions between the high symmetry Γ–M and Γ–K directions. From equation (3) we calculated the line shapes of the E′ and $A_1'$ modes of 1L $WS_2$ NCs. It is noteworthy that the physical origin of phonon confinement effect is same for the two modes, and therefore, the same confinement coefficient $\alpha$ must be used for both the E′ and $A_1'$ modes in 1L $WS_2$ NCs. We found that $\alpha = 8$ gives a good fitting to the profile and peak shift of the $A_1'$ mode for all the 1L $WS_2$ NCs, and the representative fitting results for #2-NCa and #7-NCa are shown in figure 2(b), and the corresponding domain size $L_D$ are 10 nm and 2.3nm, respectively. However, for the E′ mode, its asymmetric tail extends down to about 335 $cm^{-1}$, and two additional modes must be included to get a good fit to the E′ profile, as had done in the case of 1L $MoS_2$ NCs [4, 18]. The origin of the new modes activated by the ion-implantation will be discussed later.

Figure 2(c) shows the phonon dispersion of 1L $WSe_2$ [31]. It is quite different from that of 1L $WS_2$. For example, in contrast to 1L $WS_2$, the $ZO_2$ branch of 1L $WSe_2$ increases in frequency away from Γ. The RWL model is also used to understand the E′ and $A_1'$ modes of 1L $WSe_2$ NCs produced by ion implantation. Because the $A_1'$ mode is much stronger than the E′ mode, their intensity ratio (1/8) keeps as a constant in the fitting. $\alpha = 5$ gives a good fitting to the peak position of the $A_1'$ mode and the fitted domain sizes $L_D$ are 14 nm and 4 nm for #2-NCb and #7-NCb,

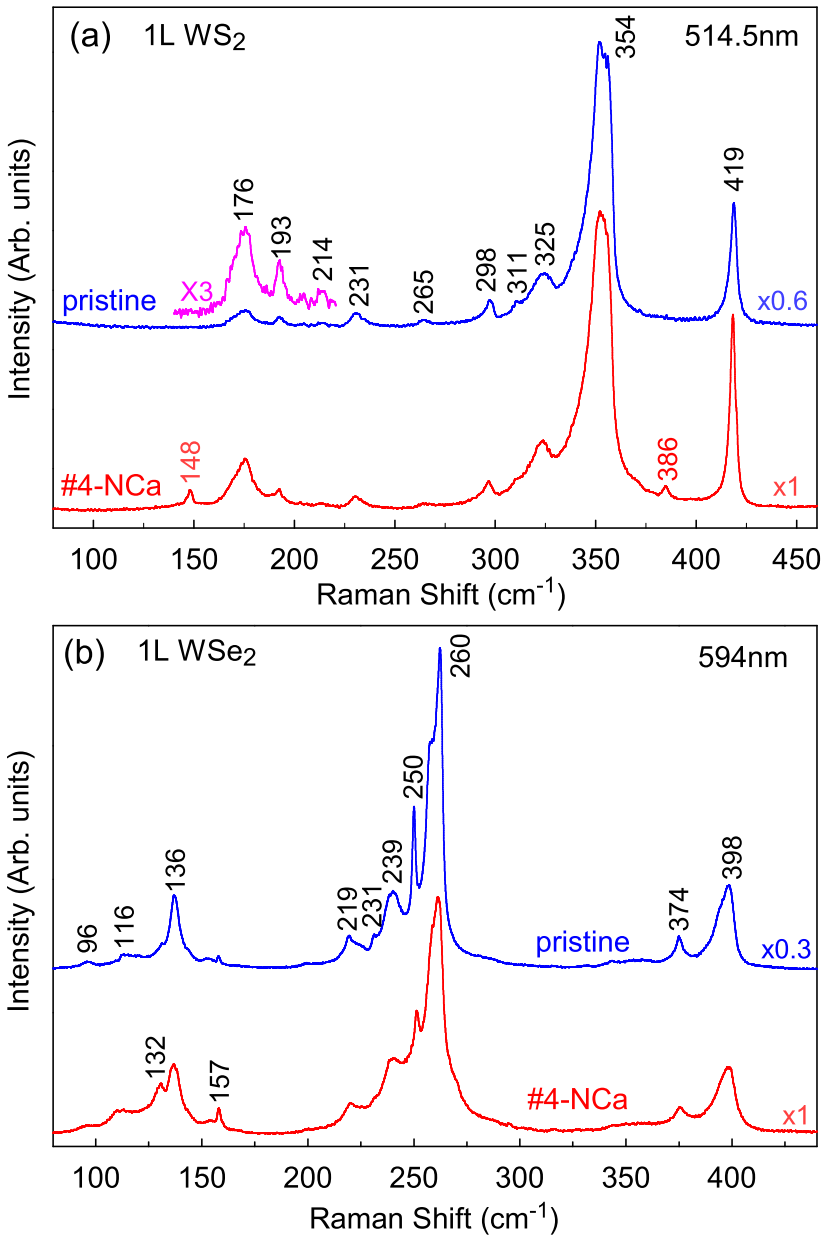


**Figure 3.** (a) Resonant Raman spectra of pristine (blue) and ion-implanted (red) (a) 1L $WS_2$ and (b) 1L $WSe_2$ at room temperature. The peak position of each mode is labeled.

respectively. The representative fitting results are shown in figure 2(d). In contrast to the Raman spectra of pristine 1L $WSe_2$, additional modes are also observed in the spectral range of the $A_1'$ mode. The origin of the new modes in 1L $WSe_2$ NCs will be also discussed later. When the domain size decreases from 14 to 4 nm, the $A_1'$ mode shows a blueshift of 1.7 $cm^{-1}$ with a broadening of 2.4 $cm^{-1}$. It is clear that the opposite trend of phonon frequency away from Γ of the $ZO_2$ branch between 1L $WS_2$ and 1L $WSe_2$ results in the opposite shift of the $A_1'$ mode in the corresponding NCs with increasing the ion dosage.

The phonon modes of 1L $WS_2$ and 1L $WSe_2$ have been well known based on the theoretical and experimental studies [4, 19, 30, 31]. Therefore, the new modes observed in the Raman spectra of ion-implanted 1L $WS_2$ and 1L $WSe_2$ mainly originate from phonons away from Γ with high density of states. The first-order phonon mode can be activated by the relaxation of selection rule by disorders or finite domain size. The fundamental $q \sim 0$ selection rule can be fulfilled for overtone and two-phonon combination modes by combining two phonons with opposite wavevectors. Although both of them are usually weak, they can be significantly enhanced in intensity and be clearly observed in the Raman experiments under the resonant condition [32]. There are two kinds of the two-phonon combination modes, i.e., the subtraction mode and addition mode. If the frequency of two fundamental modes is $\omega_1$ and $\omega_2$ ($\omega_1 > \omega_2$), the frequency of the subtraction mode and addition mode is $\omega_1 - \omega_2$ and $\omega_1 + \omega_2$. The intensity of a two-phonon

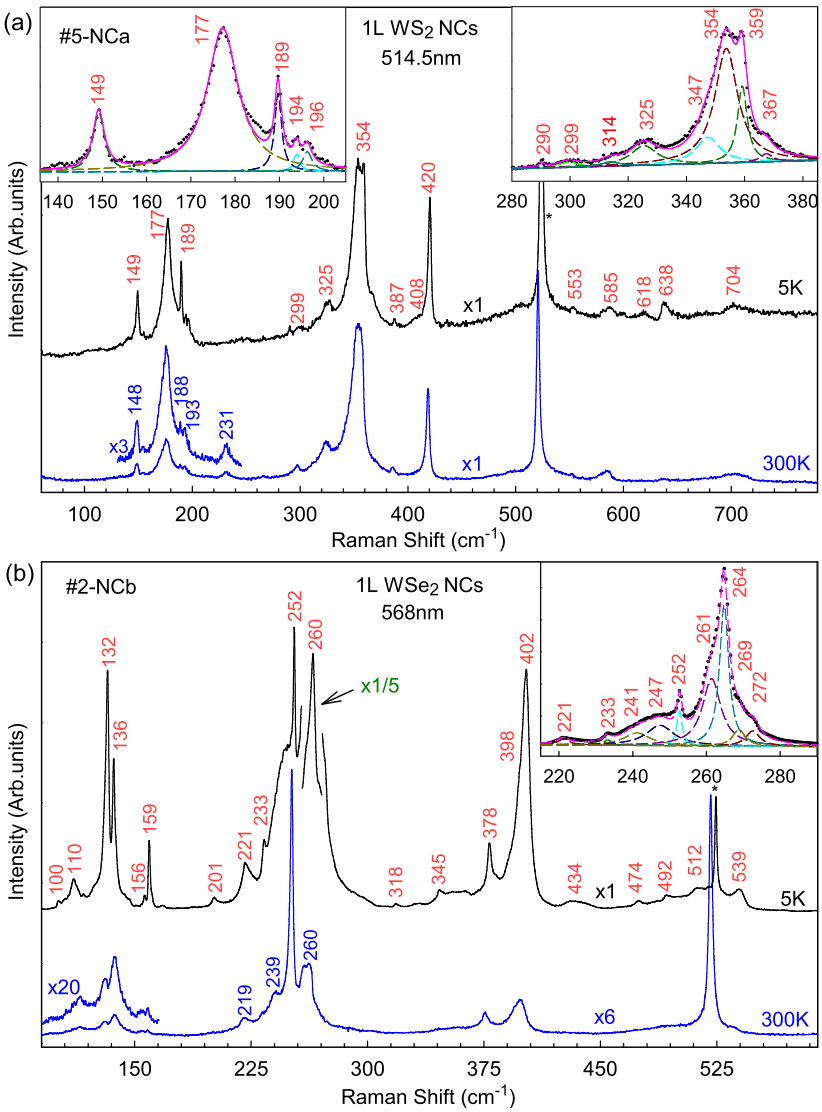


**Figure 4.** Resonant Raman spectra at 5 K (black solid lines) and 300 K (Blue solid lines) of (a) 1L $WS_2$ NCs and (b)1L $WSe_2$ NCs. The insets show the fits to the Raman peaks at the corresponding ranges. The Si Raman peak at 520 $cm^{-1}$ is indicated by asterisk (*).

mode at $\omega_1 - \omega_2$ will be strongly dependent on temperature as $n(\omega_1, T)[n(\omega_2, T) + 1]$ for creation of a phonon $\omega_2$ and annihilation of $\omega_1$, where $n(\omega, T) = (e^{\hbar\omega/kT} - 1)^{-1}$ is the phonon occupation probability [10]. Therefore, Raman spectrum at low temperature can be used for the identification of two-phonon subtraction mode [4, 33]. Therefore, in order to reveal the new modes appearing in 1L $WS_2$ and 1L $WSe_2$ after ion implantation, we measured the corresponding Resonant Raman spectra and low-temperature Raman spectra.

As the 514.5 nm (2.41 eV) excitation is close to the B exciton for 1L $WS_2$, [34] it is used to probe the resonant Raman spectra of pristine and ion-implanted 1L $WS_2$ at room temperature, as shown in figure 3(a). The non-resonant Raman spectra of pristine 1L $WS_2$ is dominated by $E'$ and $A_1'$ modes, while under the resonant condition, more intense modes are found at ~176 $cm^{-1}$, ~193 $cm^{-1}$, ~204 $cm^{-1}$, ~214 $cm^{-1}$, ~231 $cm^{-1}$, ~265 $cm^{-1}$, ~298 $cm^{-1}$, ~311 $cm^{-1}$, ~325 $cm^{-1}$. The most remarkable feature is the intensity enhancement of Raman peak at ~353 $cm^1$, which overlaps with the $E'$ mode. Similar results have been reported and some of them have been assigned [4, 19, 35]. For ion-implanted 1L $WS_2$, some additional modes arise because of the relaxation of Raman selection rule in the NCs. Two obvious peaks are observed at ~148 $cm^{-1}$ and ~386 $cm^{-1}$. The assignment will be done later. All the modes in the ion-implanted sample exhibit a decrease in peak intensity due to its worse crystal quality. Two peaks at ~204 $cm^{-1}$ and ~214 $cm^{-1}$ are too weak to be observed, while the peak at ~176 $cm^{-1}$ become stronger relative to the intensity of $E'$ and $A_1'$ modes. Similarly, resonant Raman spectroscopy of pristine 1L $WSe_2$ and 1L $WSe_2$ NCs are performed using a 594 nm laser line at room temperature, as shown in figure 3(b). There are no additional modes appear in ion-implanted 1L $WSe_2$ with respect to the pristine one. However, relative to the mode at 260 $cm^{-1}$, several modes become

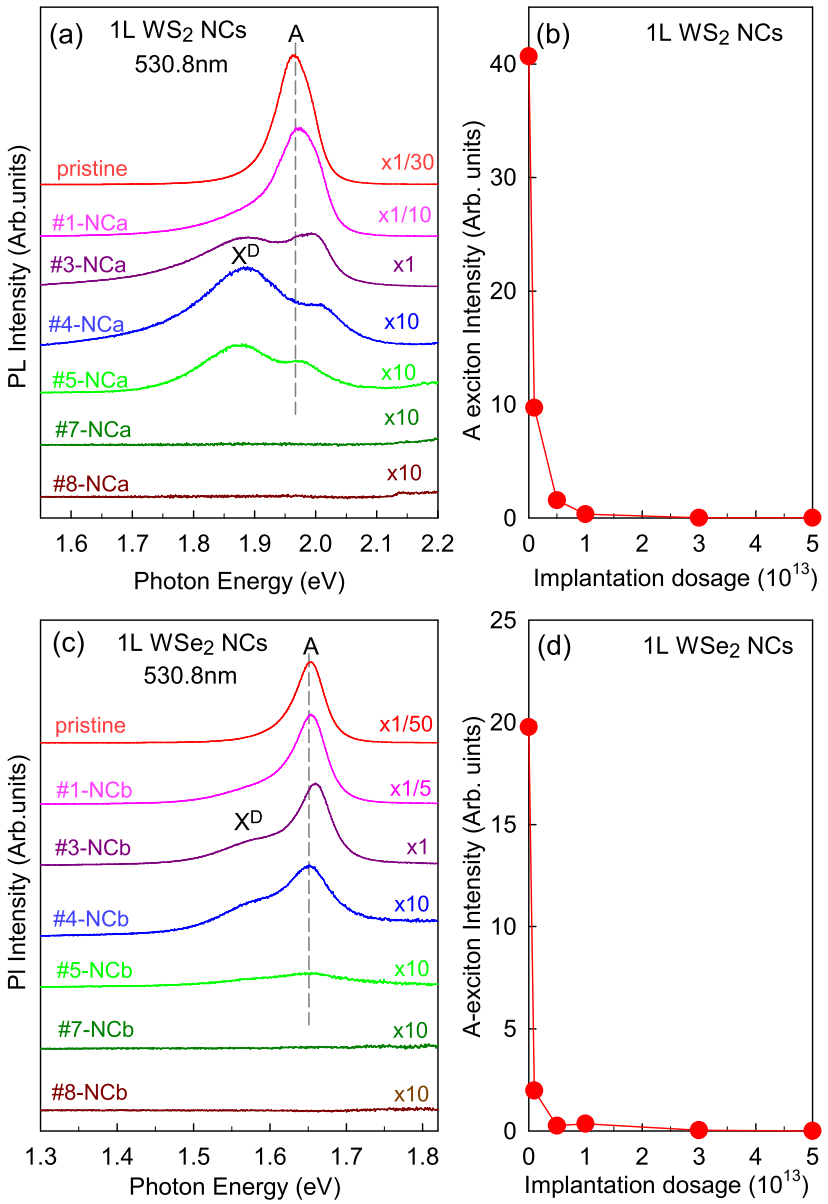


**Figure 5.** (a) PL spectra of 1L $WS_2$ subjected to different ion dosages and (b) the A-exciton intensity as a function of ion dosage. (c) PL spectra of 1L $WSe_2$ subjected to different ion dosages and (d) the A-exciton intensity as a function of ion dosage.

stronger in intensity after ion-implantation. In the spectral region between 80 and 175 $cm^{-1}$, the peak at 132 $cm^{-1}$ is too weak to be observed in pristine 1L $WSe_2$, but is clearly observed in ion-implanted one. The peak at ~157 $cm^{-1}$ can be obviously resolved from the background signal.

Based on the frequency match between the experimental values and the theoretical ones from the calculated phonon dispersion curves, one can assign the observed one-phonon Raman modes at zone center and zone edge, the overtone of the fundamental modes and the two-phonon subtraction and addition modes. To identify the the two-phonon subtraction and addition modes, resonant Raman spectra of 1L $WS_2$ NCs and 1L $WSe_2$ NCs are measured at 300 and 5 K, as shown in figures 4(a) and (b), respectively. The Raman modes at 5 K show a blueshift relative to the corresponding modes at 300 K, and the two-phonon subtraction mode should vanish at 4 K. For simplicity, the peak positions mentioned below refer to the peaks at 5 K. The Raman peak of Si from substrate is indicated by asterisk in figure 4. Most of the Raman peaks in pristine 1L $WS_2$ and 1L $WSe_2$ have been assigned previously based on the results at room temperature [4, 19, 36]. The peak at ~177 $cm^{-1}$ in 1L $WS_2$ is previously attributed to a two-phonon subtraction mode of $E'(M)^{TO_2}$-LA(M) [19, 36]. It was also assigned to the LA(M) mode recently [35]. Besides, the peak at ~149 $cm^{-1}$ in 1L $WS_2$ NCs can be denoted as ZA(M) or $E''(M)^{TO_1}$-LA(M) based on frequency match and the phonon dispersion [30]. Based on the presence of the peaks at 149 and 177 $cm^{-1}$ at 5K, the two modes are assigned as ZA(M) and LA(M), rather than $E''(M)^{TO_1}$-LA(M) and $E'(M)^{TO_2}$-LA(M), respectively. The peak at ~231 $cm^{-1}$ disappears at 5 K, confirming its assignment of $A_1'$(M)-LA(M) [35]. Similarly, for 1L $WSe_2$,

**Table 1.** The assignment of each Raman mode observed in the resonant Raman spectra of 1L $WS_2$ NCs and 1L $WSe_2$ NCs based on phonon dispersion curves [30, 31] and frequency match. All peak positions are in $cm^{-1}$.

| 1L $WS_2$ NCs | | | 1L $WSe_2$ NCs | | |
|---|---|---|---|---|---|
| 300 K | 5 K | Assignment | 300 K | 5 K | Assignment |
| 148 | 149 | ZA(M) | | 100 | TA(M) |
| 176 | 177 | LA(M)[a] | | 110 | ZA(M) |
| 188 | 189 | LA(K)[b] | 131 | 132 | LA(M) |
| 193 | 194 | | 136 | 136 | |
| | 196 | | 157 | 159 | |
| 231 | 232 | $A_1'$(M) − LA(M)[a] | | 201 | 2TA(M) |
| | 290 | 2ZA(M) | 219 | 221 | TA(M) + ZA(M)[c] |
| 298 | 299 | E″(Γ)[c] | 231 | 233 | LA(M) + TA(M) |
| 311 | 314 | LA(M) + TA(M) | 239 | 242 | LA(M) + ZA(M)[c] |
| 324 | 325 | $E''(M)^{TO_1}$[c] | 245 | 247 | $E'(M)^{LO_2}$ |
| 345 | 347 | $E'(M)^{TO_2}$[c] | 250 | 252 | E′(Γ) $A_1'$(Γ)[c] |
| 353 | 354 | 2LA(M)[a] | 258 | 261 | $A_2''$(M)[c] |
| 357 | 359 | E′(Γ)[a] | 261 | 264 | 2LA(M)[d] |
| | 367 | $E'(M)^{LO_2}$ | 263 | 269 | $A_1'$(M)[c] |
| 385 | 387 | $A_2'$(M) | | 272 | |
| | 408 | $A_1'$(M) | | 318 | $E''(M)^{LO_1}$ + TA(M) |
| 418 | 420 | $A_1'$(Γ)[a] | | 345 | $E'(M)^{LO_2}$ + TA(M) |
| | 553 | $A_1'$(M) + ZA(M) | 375 | 378 | $E'(M)^{LO_2}$ + LA(M)[d] |
| 583 | 585 | $A_1'$(M) + LA(M)[a] | 394 | 398 | 3LA(M)[d] |
| | 618 | $E''(M)^{LO_1}$ + 2LA(M) | 398 | 402 | $A_1'$(M) + LA(M)[d] |
| | 638 | $E''(M)^{LO_1}$ + 2ZA(M) | | 434 | $E'(M)^{LO_2}$ + 2TA(M) |
| 702 | 704 | 4LA(M)[a] | | 474 | $E'(M)^{LO_2}$ + 2ZA(M) |
| | | | | 492 | $E'(M)^{TO_2}$ + 2LA(M) |
| | | | | 512 | $E'(M)^{LO_2}$ + 2LA(M) |
| | | | 535 | 539 | 2$A_1'$(M)[c] |

[a] Reference [35].
[b] Reference [37].
[c] Reference [4].
[d] Reference [19].

**Table 2.** The domain size ($L_D$) of 1L $WS_2$ NCs and 1L $WSe_2$ NCs prepared by ion implantation with different ion dosages. The fitted $\alpha$ are 8 and 5 for 1L $WS_2$ NCs and 1L $WSe_2$ NCs, respectively.

| Ion dosage | $1 \times 10^{12}$ | $5 \times 10^{12}$ | $1 \times 10^{13}$ | $3 \times 10^{13}$ | $5 \times 10^{13}$ | $8 \times 10^{13}$ | $1 \times 10^{14}$ |
|---|---|---|---|---|---|---|---|
| $L_{D,WS_2}$(nm) | 12 | 10 | 8 | 6 | 5 | 3 | 2.3 |
| $L_{D,WSe_2}$(nm) | 16 | 14 | 11 | 9 | 6 | 5 | 4 |

the peaks ~136 and ~159 $cm^{-1}$ can not be assigned as $A_1'$(M)-LA(M) and $E'(M)^{LO_2}$-TA(M). Detailed fitting of the resonant peaks at 5 K near the LA(M) and E′ peaks in 1L $WS_2$ are shown in the left and right insets of figure 4(a), respectively. The corresponding fitting of the resonant peaks near the E′ peak in 1L $WSe_2$ are shown in the inset of figure 4(b). The assignment of the observed modes in 1L $WS_2$ and 1L $WSe_2$ based on the frequency match and the corresponding phonon dispersion curves is summarized in table 1.

Defect engineering had been used to modulate the optical properties of TMDs, and the strong and stable PL emission from defect sites had been realized in 1L $MoS_2$ [38]. We performed micro-PL measurements of 1L $WS_2$ and 1L $WSe_2$ NCs to probe the role of defects on the corresponding PL spectra. Figure 5(a) shows the representative PL spectra of 1L $WS_2$ under different ion dosages. The dependence of A exciton intensity on the ion dosage is summarized in figure 5(b). The PL spectrum of pristine 1L $WS_2$ is dominated by A exciton (~2 eV), which exhibits significant intensity enhancement relative to bulk $WS_2$ because of its direct band-gap semiconductor. The ion implantation can induce some defects and disordered structures in 1L $WS_2$, which can act as carrier trapping center and weaken the PL intensity of the A exciton. Indeed, even the ion dosage is as small as $1 \times 10^{12}$ (#1-NCa), the A exciton intensity shows a sharp decrease while the corresponding Raman spectrum is very similar to that of the pristine one. With increasing ion dosage, the PL intensity continues to decrease. The larger the implantation ion dosage is, the worse the crystal quality of 1L $WS_2$ is and NCs act as efficient carrier trapping centers and quench the PL emission from 1L $WS_2$ NCs. When the ion dosage increases up to $1 \times 10^{14}$ (#7-NCa), the PL

emission from 1L $WS_2$ NCs completely vanishes. However, the Raman feature is preserved with half intensity of the $A_1'$ mode observed in pristine 1L $WS_2$ (see figure 1(a)). This means that the crystal quality of 1L $WS_2$ NCs is not so bad although the corresponding PL emission is quenched by the carrier trapping centers. Thus, PL emission from A exciton is highly sensitive to the crystal quality while Raman spectroscopy is very sensitive to detect the presence of TMD NCs in the sample. Another feature in 1L $WS_2$ NCs is that the PL emission of the A exciton blueshifts with decreasing domain size of 1L $WS_2$ NCs, as indicated by the dashed line in 5(a). This is attributed to the quantum confinement effect of the A exciton in 1L $WS_2$ NCs, which have been widely observed in semiconductor quantum wells, wires and dots [39]. On the other hand, the defects in 1L $WS_2$ induced by ion implantation introduce a new peak ($X^D$) near ~1.88 eV, and its intensity relative to A exciton increases with increasing ion dosage. This peak is attributed to PL emission from defect-bound neutral excitons. Similar peaks had been observed in 1L $WS_2$ and 1L $MoS_2$ using plasma treatments [6]. The intensity of $X^D$ relative to the A exciton increases up to a maximum in #4-NCa with ion dosage of $3 \times 10^{13}$, and then decreases and finally vanishes along with the A exciton. Therefore, the $X^D$ intensity relative to the A exciton can also be used as a signature of crystal quality of 1L $WS_2$. Figure 5(c) shows the representative PL spectra of 1L $WSe_2$ under different ion dosages, and the dependence of A exciton intensity on the ion dosage is summarized in figure 5(d). Similar results are obtained. The confinement effect of the A exciton in 1L $WSe_2$ NCs is less significant than that in 1L $WS_2$ NCs.

## 4. Conclusion

In summary, we report on the Raman and PL spectra of 1L $WS_2$ and 1L $WSe_2$ NCs produced by ion implantation. Although $WS_2$ and $WSe_2$ are typical TMDs with same crystal symmetry, their $A_1'$ of NCs exhibit opposite peak shift and asymmetric profile relative to the modes of pristine crystals, which can be well understood by phonon dispersion trend of the corresponding phonon branches away from Γ and the quantum confinement effect of phonons in the Raman scattering. This provides us a method to probe the trend of a phonon branches away from Γ for 2D materials and further for other materials. Several phonons from BZ boundary are observed in the Raman spectra of NCs, and are further confirmed by resonant Raman measurements at low temperature. For the PL study of 1L $WS_2$ and 1L $WSe_2$ NCs, a peak originates from defect-bound excitons is observed below A-exciton peak, and its intensity relative to A exciton increases with increasing ion dosage. It is found that PL emission from A exciton is highly sensitive to the crystal quality while Raman spectroscopy is very sensitive to detect the presence of TMD NCs in the sample. Our results not only provide a simple method to detect the crystal quality of 2D materials, but also offer a route toward tailoring the optical properties of 2D materials by controllable defect engineering.

## Acknowledgments

This work was supported by the National Natural Science Foundation of China, Grant Nos. 11225421, 11434010, 11474277, and 11574305. J. Z. acknowledge financial support from the National Young 1000 Talent Plan.

## References

[1] Mak K F, Lee C, Hone J, Shan J and Heinz T F 2010 *Phys. Rev. Lett.* **105** 136805
[2] Chhowalla M, Shin H S, Eda G, Li L J, Loh K P and Zhang H 2013 *Nat. Chem.* **5** 263–75
[3] Wang Q H, Kalantar-Zadeh K, Kis A, Coleman J N and Strano M S 2012 *Nat. Nanotechnol.* **7** 699–712
[4] Zhang X, Qiao X F, Shi W, Wu J B, Jiang D S and Tan P H 2015 *Chem. Soc. Rev.* **44** 2757–85
[5] Tongay S *et al* 2013 *Sci. Rep.* **3** 2657
[6] Chow P K, Jacobs-Gedrim R B, Gao J, Lu T M, Yu B, Terrones H and Koratkar N 2015 *ACS Nano* **9** 1520–7
[7] Asari E, Kamioka I, Nakamura K G, Kawabe T, Lewis W A and Kitajima M 1994 *Phys. Rev.* B **49** 1011–5
[8] Ishioka K, Nakamura K G and Kitajima M 1995 *Phys. Rev.* B **52** 2539–42
[9] Richter H, Wang Z and Ley L 1981 *Solid State Commun.* **39** 625–9
[10] Chen J M and Wang C S 1974 *Solid State Commun.* **14** 857–60
[11] Comas F, Trallero-Giner C and Riera R 1989 *Phys. Rev.* B **39** 5907–12
[12] Zi J, Zhang K M and Xie X D 1997 *Phys. Rev.* B **58** 6712–5
[13] Arora A K, Rajalakshmi M, Ravindran T R and Sivasubramanian V 2007 *J. Raman Spectrosc.* **38** 604–17
[14] Gouadec G and Colomban P 2007 *Prog. Cryst. Growth Charact. Mater.* **53** 1–56
[15] Martins Ferreira E H, Moutinho M V O, Stavale F, Lucchese M M, Capaz R B, Achete C A and Jorio A 2010 *Phys. Rev.* B **82** 125429
[16] Adu K, Williams M, Reber M, Jayasingha R, Gutierrez H and Sumanasekera G 2012 *J. Nanotechnol.* **2012** 18
[17] Gołasa K, Grzeszczyk M, Binder J, Bożek R, Wysmolek A and Babiński A 2015 *AIP Adv.* **5** 077120
[18] Mignuzzi S, Pollard A J, Bonini N, Brennan B, Gilmore I S, Pimenta M A, Richards D and Roy D 2015 *Phys. Rev.* B **91** 195411
[19] Zhao W J, Ghorannevis Z, Amara K K, Pang J R, Toh M, Zhang X, Kloc C, Tan P H and Eda G 2013 *Nanoscale* **5** 9677–83
[20] Sun L F *et al* 2013 *Phys. Rev. Lett.* **111** 126801
[21] Chakraborty B, Matte H, Sood A K and Rao C N R 2013 *J. Raman Spectrosc.* **44** 92–6
[22] Fan J H, Gao P, Zhang A M, Zhu B R, Zeng H L, Cui X D, He R and Zhang Q M 2014 *J. Appl. Phys.* **115** 053527
[23] Lee J U, Park J, Son Y W and Cheong H 2015 *Nanoscale* **7** 3229–36
[24] Mcdevite N T, Zabinski J S, Donley M S and Bultman J E 1994 *Appl. Spectroc.* **48** 733–6
[25] Qiao X F, Li X L, Zhang X, Shi W, Wu J B, Chen T and Tan P H 2015 *Appl. Phys. Lett.* **106** 223102
[26] Tan P H, Deng Y and Zhao Q 1998 *Phys. Rev.* B **58** 5435–9
[27] Li Q Q, Zhang X, Han W P, Lu Y L, Shi W, Wu J B and Tan P H 2015 *Carbon* **85** 221–4

[28] Campbell I H and Fauchet P M 1986 *Solid State Commun.* **58** 739–741
[29] Zi J, Zhang K and Xie X 1997 *Phys. Rev.* B **55** 9263–6
[30] Molina-Sánchez A and Wirtz L 2011 *Phys. Rev.* B **84** 155413
[31] Terrones H *et al* 2014 *Sci. Rep.* **4** 4215
[32] Tan P H, Xu Z Y, Luo X D, Ge W K, Zhang Y, Mascarenhas A, Xin H P and Tu C W 2006 *Appl. Phys. Lett.* **89** 101912
[33] Golasa K, Grzeszczyk M, Leszczynski P, Faugeras C, Nicolet A A L, Wysmolek A, Potemski M and Babinski A 2014 *Appl. Phys. Lett.* **104** 092106
[34] Zhao W J, Ghorannevis Z, Chu L, Toh M, Kloc C, Tan P H and Eda G 2013 *ACS Nano* **7** 791–7
[35] Berkdemir A *et al* 2013 *Sci. Rep.* **3** 1755
[36] Frey G L, Tenne R, Matthews M J, Dresselhaus M S and Dresselhaus G 1998 *J. Mater. Res.* **13** 2412–7
[37] Peimyoo N, Shang J, Yang W, Wang Y, Cong C and Yu T 2014 *Nano Res.* **8** 1210–21
[38] Nan H Y *et al* 2014 *ACS Nano* **8** 5738–45
[39] Yu P Y and Cardona M 2005 *Fundamentals of Semiconductors: Physics and Materials Properties* (Berlin: Springer) 3rd rev